RSC Advances

PAPER

View Article Online
View Journal | View Issue

Cite this: *RSC Adv.*, 2024, **14**, 4518

SiO_2@AuAg/PDA hybrid nanospheres with photothermally enhanced synergistic antibacterial and catalytic activity†

Dazheng Ci,[a] Ning Wang,*[a] Yunqi Xu,[b] Shanshan Wu,[c] Jing Wang,[a] Haoran Li,[c] Shouhu Xuan [b] and Qunling Fang *[a]

Wastewater discharged from industrial, agricultural and livestock production contains a large number of harmful bacteria and organic pollutants, which usually cause serious harm to human health. Therefore, it is urgent to find a "one-stone-two-birds" strategy with good antimicrobial and pollutant degradation activity for treating waste water. In this paper, SiO_2@AuAg/Polydopamine (SiO_2@AuAg/PDA) core/shell nanospheres, which possessed synergistic "Ag^+-release–photothermal" antibacterial and catalytic behaviors, have been successfully prepared *via* a simple *in situ* redox polymerization method. The SiO_2@AuAg/PDA nanospheres showed good catalytic activity in reducing 4-nitrophenol to 4-aminophenol (0.576 min^{-1} mg^{-1}). Since the AuAg nanoclusters contain both gold and silver elements, they provided a high photothermal conversion efficiency (48.1%). Under NIR irradiation (808 nm, 2.5 W^{-2}), the catalytic kinetics were improved by 2.2 times. Besides the intrinsic Ag^+-release, the photothermal behavior originating from the AuAg bimetallic nanoclusters and the PDA component of SiO_2@AuAg/PDA also critically improved the antibacterial performance. Both *E. coli* and *S. aureus* could be basically killed by SiO_2@AuAg/PDA nanospheres at a concentration of 90 μg mL^{-1} under NIR irradiation. This "Ag^+-release–photothermal" coupled sterilization offers a straightforward and effective approach to antimicrobial therapy, and further exhibits high potential in nanomedicine for combating bacterial contamination in environmental treatment and biological fields.

Received 7th November 2023
Accepted 3rd January 2024

DOI: 10.1039/d3ra07607e

rsc.li/rsc-advances

1. Introduction

Over the past decade, the water pollution caused by the effects of industrial, agricultural and livestock production and urban residential water use has become increasingly prominent, and the accumulation of harmful bacteria and pollutants in wastewater poses a serious threat to people's lives.[1–4] To treat the bacteria, antibiotics are often overused; hence, the emergence and spread of super-resistant bacteria have caused a series of therapeutic problems.[5–7] In recent years, nanoplatforms have been widely investigated and demonstrated to be effective in the fields of nanocatalysis and antimicrobials. Among them, noble-metal nanocrystals (Pd, Au, Ag, Pt and Ce) have attracted more and more attention due to their simple synthesis, excellent photothermal conversion capability, good catalytic activity, and significant antimicrobial properties.[8–11] Due to their large surface area, noble-metal bimetallic nanocrystals have been widely used in the degradation of organic pollutants.[12–15] Therefore, nanoplatforms integrated with noble-metal nanocrystals possess great potential in both nanocatalysis and antimicrobials.

The organic pollutant 4-nitrophenol is carcinogenic, teratogenic, and mutagenic, and its reduction product (4-aminophenol) is widely used in a variety of applications, such as anticorrosive lubrication and corrosion inhibition, because of its low toxicity. Therefore, it is necessary to convert 4-nitrophenol to 4-aminophenol. Noble-metal nanoparticles (Au, Ag, Cu, Pt and Pd) have been commonly applied as nanocatalysts to address this problem. Liao *et al.* investigated the reduction of 4-nitrophenol by three efficient silver-based nanoparticle catalysts and found that smaller silver-nanoparticle sizes and sharper edge and corner contributed to an increase in the total surface area, which improved the catalytic performance.[16] Deshmukh *et al.* investigated and compared the effect of gold nanoparticles (AuNPs) and gold nanoflowers (AuNFs) on the reduction of 4-nitrophenol. The results showed that the AuNFs' catalytic activity was 1.57 times higher than that of AuNPs.[17] Moreover, noble-metal nanoparticles exhibit significantly enhanced catalytic activity and selectivity due to synergistic effects as well as *in situ* formation of

[a]*School of Food and Biological Engineering, Hefei University of Technology, Hefei, 230009, PR China. E-mail: nwangcn@163.com; fql.good@hfut.edu.cn; Fax: +86-551-62904353; Tel: +86-151-55934837; +86-551-62904353*

[b]*CAS Key Laboratory of Mechanical Behavior and Design of Materials, Department of Modern Mechanics, University of Science and Technology of China, Hefei 230027, PR China*

[c]*School of Materials and Chemical Engineering, Anhui Jianzhu University, Hefei, PR China*

† Electronic supplementary information (ESI) available. See DOI: https://doi.org/10.1039/d3ra07607e

reactive species.[18,19] It has been reported that a bimetallic structure facilitates the adsorption of reactants and the release of products, thus improving the catalytic performance.[20] In addition, Ag ions are known to have broad-spectrum antimicrobial activity and they can bind to the catabolic metabolite control proteins of *Staphylococcus aureus*, inducing oligomerization as well as inhibiting the ability to bind to DNA.[21] Therefore, Ag-doped bimetallic nanocrystals have broad application prospects in both antimicrobials and nanocatalysis.

Photothermal therapy (PTT) has received increasing attention as an effective, novel, non-invasive therapeutic technique that shows great potential in the treatment of drug-resistant bacteria and bacterial biofilms.[22–24] It is well-known that Au-based nanocrystals have excellent photothermal conversion effects.[25–27] In addition, noble-metal nanostructures have high photothermal conversion efficiency due to their good near-infrared absorption properties in the localized surface plasmon resonance region.[28,29] As a result, various noble-metal nanoparticles with synergistic photothermal antimicrobial performance have been explored. Furthermore, a previous report indicated that bimetallic nanocrystals had stronger antimicrobial effects than monometallic ones.[30] Kim found that Ag nanoparticles in cobalt–silver bimetallic nanocomposites exhibited strong photothermal conversion efficiency, which synergized with Ag and Co ions to achieve a significant antimicrobial effect.[31] Although Ag^+ is effective in killing bacteria as a broad-spectrum antimicrobial agent, the severe biotoxicity also limits its application. Therefore, a bio-safe nanoplatform that not only balances the biocompatibility and toxicity but also possesses controllable photothermal antibacterial behavior is highly required. Polydopamine (PDA) possesses extraordinary adhesive properties, good biocompatibility, and excellent photothermal conversion ability. During the past decades, PDA has been used to carry noble-metal nanoparticles and this method not only solves the agglomeration problem of nanocrystals but also effectively promotes the photothermal antimicrobial effect.[32–35]

Another strategy to the prevent agglomeration of noble-metal nanoparticles is to immobilize them on a carrier. It is worth noting that SiO_2 nanospheres have the advantages of high dispersibility, good chemical stability, easy modification, and high temperature resistance, which make them a non-toxic and non-polluting green material. Due to its optical transparency and biocompatibility, SiO_2 has a wide range of applications in the chemical industry, biomedicine and optoelectronic devices. SiO_2@Au and Au@SiO_2 nanoparticles have been reported to enhance the fluorescence of rhodamine B dye in the presence of AuNPs.[36] Zhang *et al.* reported that SiO_2 loaded with Pd–Cu bimetallic nanoparticles exhibited good activity and selectivity under mild conditions.[37] Similarly, metal–organic frameworks (MOFs) are a class of porous crystalline hybrid materials, and these ordered crystal structures have highly desirable physicochemical properties, such as tunable pore size, high surface area, open metal sites and large void space.[38,39] As far as applications are concerned, MOFs have a wide range of prospects in numerous fields, such as drug delivery and catalysis. To this end, the construction of bimetallic nanoplatforms based on SiO_2 or MOF carriers and investigation of their relative catalytic and antibacterial performances have become attractive.

In this study, we report a simple synthesis method for a SiO_2@AuAg/PDA nanocomposite in which the gold and silver bimetallic nanoparticles are sandwiched between SiO_2 and PDA. The content of gold and silver, as well as the thickness of the shell layer, can be controlled by changing the experimental conditions. Such noble-metal nanoparticles have catalytic and antimicrobial properties. Taking 4-nitrophenol as an example, we performed kinetic analysis experiments on the nanospheres by catalyzing its conversion to 4-aminophenol and found that the reduction effect was more significant under near-infrared irradiation. In addition, the SiO_2@AuAg/PDA composite was effective in the sterilization of Gram-negative (*Escherichia coli*, *E. coli*) and Gram-positive (*Staphylococcus aureus*, *S. aureus*) bacteria under NIR irradiation, and showed a typical "photothermal–Ag^+-release" coupled antibacterial effect. This study provides a multifunctional composite material with both bactericidal and catalytic properties, which has promising applications in environmental treatment and biology.

2. Materials and methods

2.1 Materials

2-Methylimidazole ($C_4H_6N_2$) was purchased from Hebei Bailing Wei Ultrafine Materials Co. 3-Aminopropyltriethoxysilane (APTES) and trisodium citrate dihydrate ($C_6H_5Na_3O_7 \cdot 2H_2O$) were supplied by China Aladdin Chemical Co. Cetyltrimethylammonium bromide (CTAB), zinc acetate dihydrate ($C_4H_6O_4Zn \cdot 2H_2O$), sodium borohydride ($NaBH_4$), 4-nitrophenol ($C_6H_5NO_3$), ammonia ($NH_3 \cdot H_2O$), tetraethyl orthosilicate (TEOS), gold(III) chloride ($HAuCl_4$), and silver nitrate ($AgNO_3$) were purchased from China National Pharmaceutical Chemical Reagent Co. No experimental reagents were further purified and ultrapure water was used for the experiments.

2.2 Synthesis of SiO_2@AuAg/PDA core/shell nanospheres

Synthesis of SiO_2 nanospheres. Silica nanospheres were prepared *via* a modified Stöber method.[40] First, a round-bottom flask was filled with 50 mL ethanol, 4.9 mL distilled water and 9.3 mL ammonia, and the contents stirred at 30 °C for 30 min. Then, 5 mL TEOS was added and the reaction was carried out. 12 h later, the product was separated from the suspension, and washed with water and ethanol alternately three times to obtain SiO_2 nanospheres. Finally, SiO_2 nanosphere powder was obtained *via* vacuum drying.

Synthesis of SiO_2@AuAg/PDA core/shell nanospheres. Firstly, SiO_2 nanospheres (8.5 mg) were ultrasonically dispersed in 50 mL ethanol to obtain a homogeneous solution and a drop of APTES was added. Then, freshly prepared $AgNO_3$ solution (0.02 g mL^{-1}, 136 μL), $HAuCl_4$ (0.1 g mL^{-1}, 40 μL) and sodium citrate (15 mg) were added to form solution (1). Secondly, DA-HCl (30 mg) was added to 30 mL Tris (pH = 8.5) to form solution (2). Solution (2) was then mixed with solution (1) and the reaction was conducted under ultra-sonication. After 3 h, the product was washed with ethanol and purified water alternately three times, followed by vacuum drying at 45 °C for 12 h to obtain SiO_2@AuAg/PDA nanospheres.

Synthesis of ZIF-8@AuAg/PDA nanospheres. First, 14.4 g of $Zn(CH_3COO)_2 \cdot 2H_2O$ and 0.0384 g CTAB were dissolved in 240 mL of water, sealed and sonicated. Next, 140 mL of aqueous 2-methylimidazole (0.38 g mL^{-1}) was added. The solution turned into a milky white liquid under heating conditions in a water bath at 25 °C for 2 hours, then it was centrifuged (9000 rpm, 5 min). Finally, the solution was washed with anhydrous ethanol more than 3 times and dried in a vacuum oven for 12 h to obtain ZIF-8 nanocubes. For the preparation of ZIF-8@AuAg/PDA, ZIF-8 (10 mg) was sonicated in 40 mL ethanol for 2 h. Then, 40 μL chloroauric acid, trisodium citrate and 136 μL of a ready-made Ag ion solution were added and sonicated. Then, 30 mL Tris buffer (pH = 8.5) mixed with 30 mg of DA was added and the reaction was carried out for 3 h. Finally, ZIF-8@AuAg/PDA could be obtained by centrifugation, washing with ethanol and vacuum drying at 45 °C for 12 h.

2.3 Photothermal effect of SiO_2@AuAg/PDA

SiO_2@AuAg/PDA nanospheres were dispersed in deionized water at a concentration of 1 mg mL^{-1} and diluted into a gradient of five concentrations (20, 40, 60, 80 and 100 μg mL^{-1}). The respective absorbances of the diluted suspensions were then measured at 808 nm. Then, 1 mL SiO_2@AuAg/PDA at different concentrations was taken in a centrifuge tube (1.5 mL) and continuously irradiated with a near-infrared laser (808 nm, 2.5 W cm^{-2}) for 6 min, and the temperature at different time points was recorded with an infrared camera. In order to evaluate the light absorption capacity of the nanocatalysts at 808 nm, the extinction coefficient $\varepsilon(\lambda)$ was determined according to the Lambert–Beer law:

$$A(\lambda) = \varepsilon LC \quad (1)$$

where A is the absorbance at λ (808 nm), L is the optical length (1 cm), and C is the concentration of the aqueous SiO_2@AuAg/PDA solution (μg mL^{-1}). The extinction coefficient ε was calculated by plotting the slope (L g^{-1} cm^{-1}) of each linear fit *versus* wavelength. In addition, the photothermal conversion efficiency was calculated as follows:[41]

$$\eta = \frac{hS(T_{max} - T_{surr}) - Q_{Dis}}{I(1 - 10^{-A_{808}})} \quad (2)$$

The value of hS is obtained using the formula $m \cdot C_p = hS \cdot \tau_S$, where m is the volume of the solution, C_p is the specific heat of water and τ_S refers to a time constant of sample system. T_{max} and T_{surr} are the maximum and room temperatures, respectively, while Q_{Dis} the heat dissipation of the light absorption of the sample itself. I is the laser power and A_{808} is the absorbance value of the sample at 808 nm.

2.4 Catalytic activity of SiO_2@AuAg/PDA nanospheres for the reduction of 4-nitrophenol

First, 50 mL of aqueous 4-nitrophenol (10^{-4} M) and 50 mg $NaBH_4$ were added to a beaker (100 mL), and then SiO_2@AuAg/PDA nanospheres were added to the mixture. To monitor the reaction, 2 mL of the reaction solution was quickly removed with a syringe at regular intervals and the nanocatalysts were separated from the reaction solution by injecting them into a centrifuge tube through a pressurized syringe filter to stop the reaction. The conversion of 4-nitrophenol was then detected by UV spectrophotometry and the characteristic absorption at 400 nm was monitored. After the reaction, the nanocatalyst was separated from the reaction system by suction filtration and reused in subsequent catalytic reactions. We studied the reaction kinetics of the catalytic 4-nitrophenol degradation reaction. Typically, catalytic degradation reactions follow the Langmuir–Hinshelwood model and exhibit distinct first-order reaction kinetics (k_{app}). The apparent rate is determined using the following equation:[42,43]

$$\ln(C_0/C_t) = k_{app} \quad (3)$$

C_0 and C_t are the initial concentration of the solution and the concentration at reaction time t, respectively.

2.5 Antibacterial activity testing for SiO_2@AuAg/PDA

The antibacterial activity of SiO_2@AuAg/PDA nanospheres against *E. coli* (Gram-negative bacteria) and *S. aureus* (Gram-positive bacteria) was conducted. First, an appropriate amount (50 μL) of *E. coli* or *S. aureus* preserved in glycerol was taken out and added to 50 mL of Lauria–Bertani culture broth, placed in a conical flask and oscillated for 12 h at 37 °C and 100 rpm. The cultured bacteria were then diluted to 1×10^6 CFU mL^{-1} with broth and different concentrations of samples were added. After mixing, the bacterial suspensions were treated with a NIR laser (808 nm, 2.5 W cm^{-2}) and without a NIR laser, labeled as L^+ and L^-, respectively. The treatment time was 6 min, except for the control group. Each group was incubated in a constant-temperature incubator at 37 °C for 4 h. The diluted co-culture solution (100 μL) was inoculated on plates containing Luria–Bertani agar medium and incubated at 37 °C for 24 h. The total number of surviving bacteria was determined using the dilution method and planar colony counting.

2.6 Characterization

The morphology and nanostructure of the nanocomposites were analyzed *via* field emission transmission electron microscopy (FE-TEM) using a JEM-2100F and scanning electron microscopy (SEM) using a JEOL JSM-6700F. Energy-dispersive X-ray spectroscopy (EDS) was carried out using a JEM-2100F field emission transmission electron microscope. X-ray diffractometers (Bruker D8 Advance) were used to study the samples' X-ray powder diffraction (XRD). The infrared spectra of the samples were obtained using an infrared spectrometer (TENSOR model 27) in the range of 4000 to 500 cm^{-1} wave numbers. The X-ray photoelectron spectroscopy (XPS) of all the samples was carried out using a photoelectron spectrometer (ESCALAB 250). Thermogravimetric analysis was carried out on a thermogravimetric apparatus (DTG-60H) under air conditions at a heating rate of 10 °C min^{-1} from room temperature to 700 °C. Temperature variations during the sample photothermal

testing experiments were studied and recorded using an infrared camera (ImageIR 8325). Finally, the metal content in the composites was determined *via* inductively coupled plasma mass spectrometry (ICP-MS, PlasmaQuad 3).

3. Results and discussion

3.1 Synthesis and characterization of SiO_2@AuAg/PDA core/shell nanospheres

In this paper, SiO_2@AuAg/PDA nanospheres were successfully prepared *via* a simple *in situ* reduction–oxidation polymerization reaction.[44] Scheme 1 shows the synthesis process of the SiO_2@AuAg/PDA nanospheres. Firstly, SiO_2 nanospheres were obtained *via* the well-known sol–gel method. Then, an appropriate amount of APTES was added into the system for surface functionalization modification and the subsequent amino-modified SiO_2 nanospheres provided many anchor sites for the noble-metal nanoparticles, enhancing the interaction between the noble-metal nanoparticles and SiO_2. Finally, through a one-step *in situ* redox polymerization reaction between chloroauric acid, silver nitrate solution and dopamine hydrochloride, the AuAg/PDA hybrid layer was successfully formed and it uniformly covered the surface of the SiO_2 nanospheres, resulting in the formation of the SiO_2@AuAg/PDA hybrid nanostructure.

Fig. 1a shows the SEM image of the SiO_2@AuAg/PDA nanospheres. The final sample has a rough surface, which indicates that the AuAg nanoparticles are uniformly coated on the SiO_2 nanospheres. As shown in the TEM images, the SiO_2@AuAg/PDA nanospheres are relatively uniform in size and show a typical sandwich structure (Fig. 1b). In addition, the large magnification TEM image in Fig. 1c also demonstrates that the AuAg nanocrystals are located between the SiO_2 nanosphere and PDA shell. The synthesized samples exhibit a spherical morphology and the average particle size of the final SiO_2@AuAg/PDA is about 330 nm with a shell thickness of about 25 nm. The high magnification TEM image (Fig. 1c) shows that there is a large amount of black particles between the SiO_2 nanospheres and the PDA shell layer. As a comparison, the SiO_2/PDA nanospheres also could be obtained in the absence of $AgNO_3$ and $HAuCl_4$ (Fig. 1d–f). Different from the SiO_2@AuAg/PDA, the surface of the nanosphere is smooth. However, an obvious thin shell with a bumpy appearance is found on the surface of the solid core, which indicates that the PDA layer has been well-coated on the SiO_2 nanospheres. Fig. 1g–i are the TEM and SEM images of the pristine SiO_2 nanospheres. It is found that SiO_2 nanospheres are uniformly distributed and possess a spherical structure. Based on the above analysis, it can be concluded that hybrid nanoparticles with AuAg nanoparticles sandwiched between the SiO_2 nanosphere and PDA shell are effectively obtained.

To further analyze the internal structure of the AuAg bimetallic nanocrystals in the sandwich-structured SiO_2@AuAg/PDA nanospheres, high-angle annular dark-field scanning electron microscopy (HAADF-STEM) and energy-dispersive X-ray spectroscopy (EDX) elemental mapping studies were carried out. The average size of SiO_2@AuAg/PDA is increased by about 50 nm compared to pristine SiO_2, which originates from the AuAg/PDA coating (Fig. 2a). It is clear that the core/shell nanostructures are mainly composed of C, N, O, Si, Au and Ag (Fig. 2b). Fig. 2c–e show the dispersion of the N, O, and Si elemental composition, respectively. It is noteworthy that the Au and Ag elements are distributed in a hollow-appearing spherical shape, the sizes of which are both larger than the Si sphere (Fig. 2f and g), which indicates that the periphery of the SiO_2 nanosphere is well-encapsulated by the AuAg bimetallic nanocrystals. Moreover, the diameters of Au/Ag element spheres are smaller than that of N, suggesting that the AuAg nanocrystals are sandwiched between the SiO_2 core and the PDA layer, which is in accordance with the TEM analysis. In this work, it is found that the Au and Ag elements show the similar distribution; thus, they are defined as AuAg bimetallic

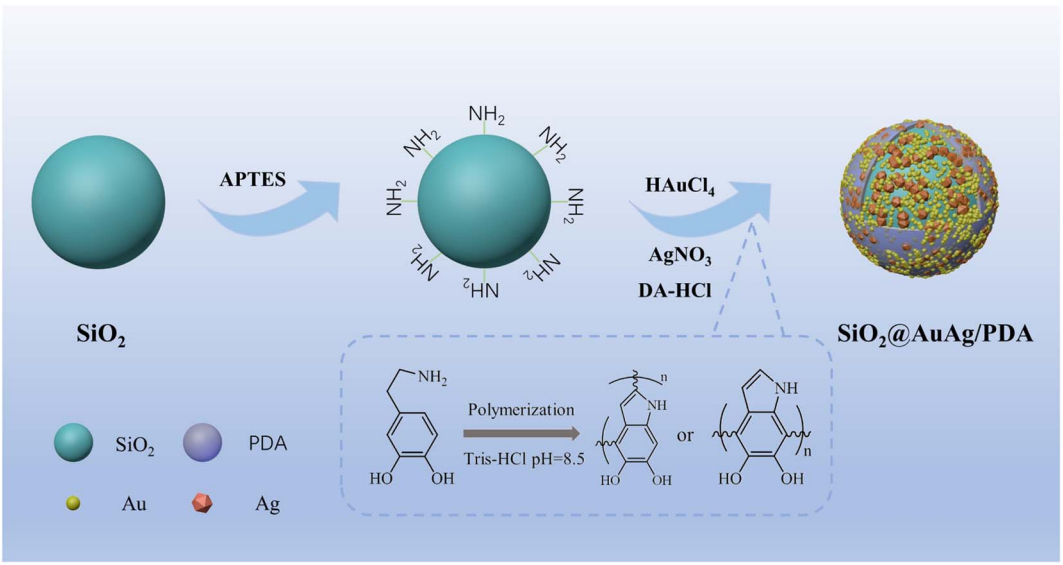

Scheme 1 Schematic illustration for the preparation of SiO_2@AuAg/PDA core/shell nanospheres.

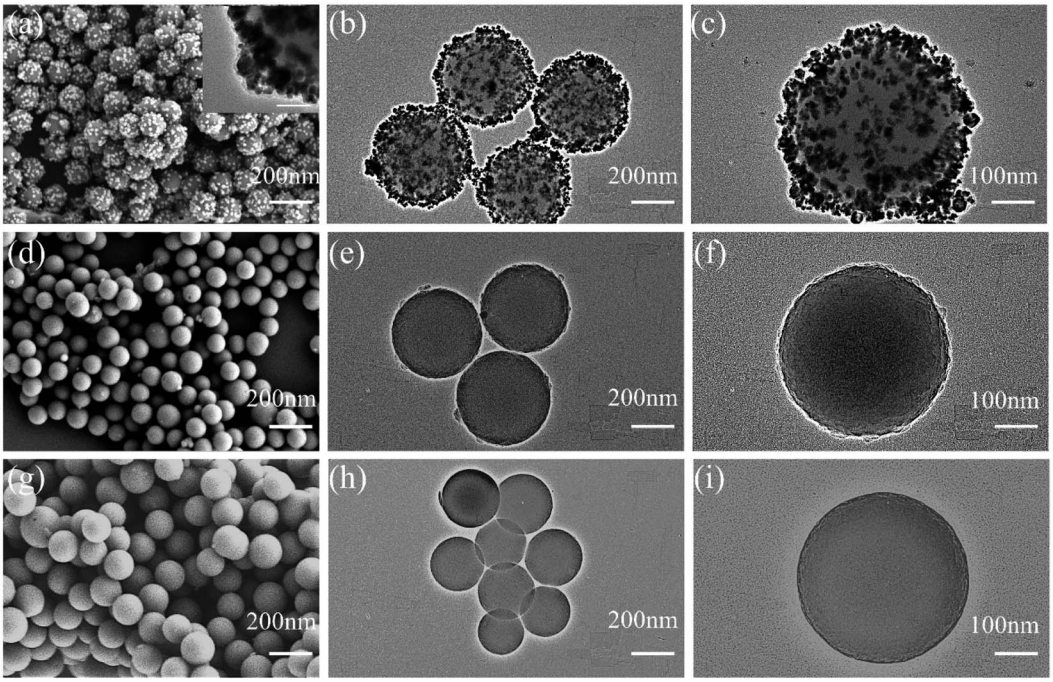

Fig. 1 SEM (a) and TEM (b and c) images of SiO_2@AuAg/PDA, SEM (d) and TEM (e and f) images of SiO_2/PDA, and SEM (g) and TEM (h and i) images of SiO_2; the scale bar of the TEM inset in (a) is 20 nm.

nanocrystals. These bimetallic nanocrystals are not uniformly distributed on the surface of SiO_2 core and most of them are assembled together to form cluster-like nanostructures. This result must be owing to the *in situ* reduction to form AuAg bimetallic nanocrystals, which will be further discussed in the following discussion. Furthermore, the EDX spectrum also matches the above analysis, which also evidences the successful preparation of SiO_2@AuAg/PDA nanospheres (Fig. 2h).

In this work, the AuAg/PDA layers are simultaneously formed on the SiO_2@AuAg/PDA nanospheres. The AuAg nanostructure and composition of SiO_2@AuAg/PDA can be easily tuned by controlling the concentrations of the precursors. Fig. S1† shows the TEM images of SiO_2@AuAg/PDA prepared using different contents of $HAuCl_4$: 0 mM (a and b), 5.94×10^{-3} mM (c and d), 8.82×10^{-3} mM (e and f) and 1.17×10^{-2} mM (g and h). Shown in Fig. S1a and b† are the products obtained without the addition of $HAuCl_4$. Clearly, most of the SiO_2 nanospheres have tiny Ag nanoparticles attached to them and some of them are naked. Our experiments indicate that the Ag nanocrystals were difficult to immobilize onto the SiO_2 nanospheres under the present conditions. When the $HAuCl_4$ content was increased from 0 mM to 5.94×10^{-3} mM, the Au/PDA layer was wrapped around the SiO_2 periphery and some AuAg nanoclusters appeared (Fig. S1c and d†). When the $HAuCl_4$ content was 8.82×10^{-3} mM, the density of the Au nanocrystals increased and many monodisperse Au nanocrystals were presented in addition to the AuAg nanoclusters (Fig. S1e and f†). On continuing to increase the $HAuCl_4$ content to 1.17×10^{-2} mM, the coverage of the SiO_2 surface was further improved and the Au nanocrystals became well-distributed (Fig. S1g and h†). The high magnification TEM images (Fig. S1b, d, f and h†) also indicate that the agglomeration of the AuAg nanocrystals gradually weakened with the increase in the $HAuCl_4$ content, which must be due to the quick reaction kinetics at high concentration and the good association between the AuAg nanocrystals and PDA polymer.

The above method can also be applied for coating of other nanocarriers due to its versatility. Here, ZIF-8@AuAg/PDA was successfully obtained by using ZIF-8 nanocubes as the template. Without using ZIF-8, only AuAg/PDA nanoaggregates were found in the product (Fig. 3a), in which the AuAg nanocrystals were encapsulated within a PDA shell. When the ZIF-8 was introduced into the reaction system composed of $HAuCl_4$, $AgNO_3$, and dopamine, ZIF-8@AuAg/PDA was fabricated *via in situ* oxidative polymerization. Fig. 3b shows the TEM image of ZIF-8, which indicates that all the products exhibit cube-like nanostructures with dimensions of around 70–130 nm. During the PDA coating, $HAuCl_4$ and $AgNO_3$ were simultaneously introduced into the ethanol suspension of ZIF-8. Ultrasonication was used to ensure that the $HAuCl_4$ and $AgNO_3$ on the ZIF-8 nanocubes were uniformly dispersed around the cubes. In addition, freshly prepared dopamine hydrochloride solution was added in Tris buffer (pH = 8.5) to start the coating process. After 3 h of sonication, ZIF-8@AuAg/PDA was successfully produced (Fig. 3c). As shown in Fig. 3d, all the ZIF-8 cubes underwent different degrees of self-etching, and there were uniform black particles between the cubes and the pale-white shells, which were obviously AuAg bimetallic nanocrystals. As a result, a ZIF-8@AuAg/PDA nanocomposite with a typical core/shell nanostructure was fabricated.

Fig. 4a shows the XRD patterns of SiO_2, SiO_2/PDA, SiO_2@Au/PDA, SiO_2@Ag/PDA and SiO_2@AuAg/PDA nanospheres. The results show that the initial SiO_2 has only one diffraction peak at

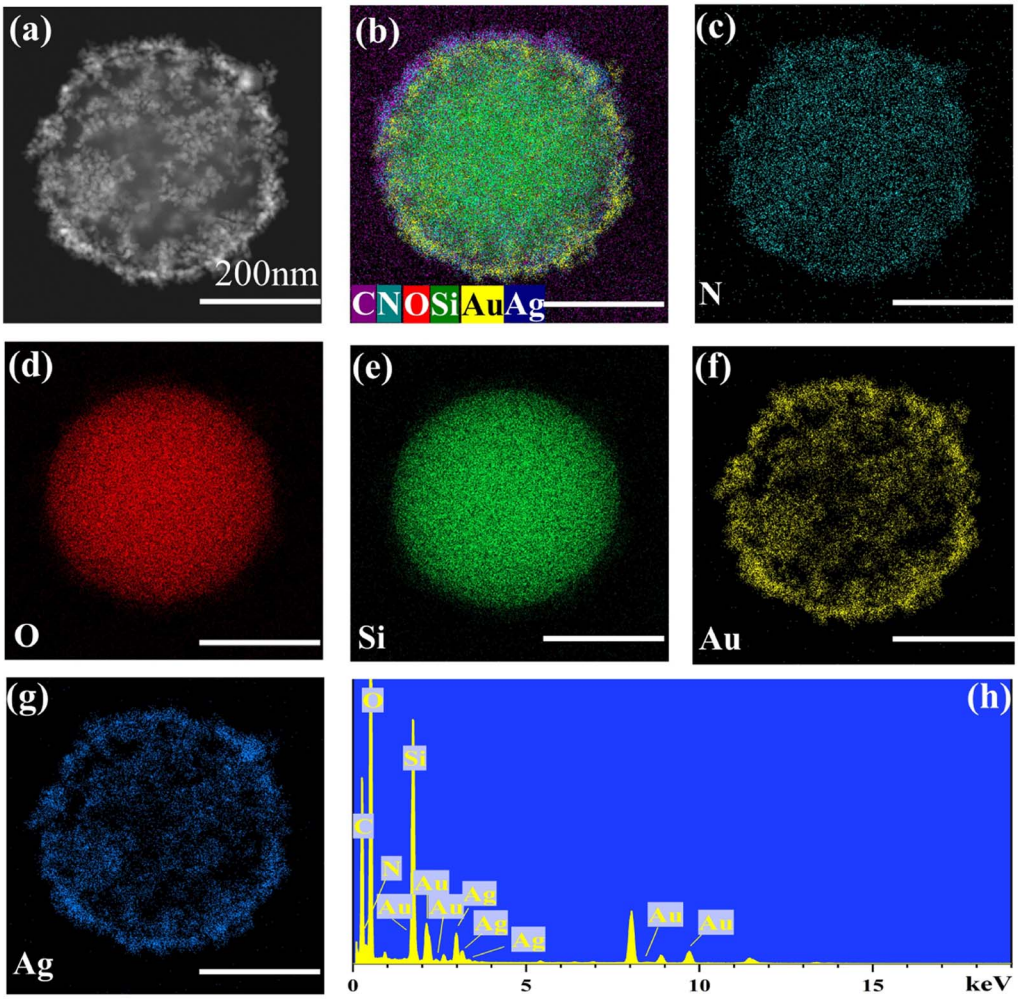

Fig. 2 HAADF-STEM images and EDX elemental mapping of C, N, O, Si, Au and Ag (a–g), and EDX spectrum of SiO_2@AuAg/PDA (h); scale bars are 200 nm.

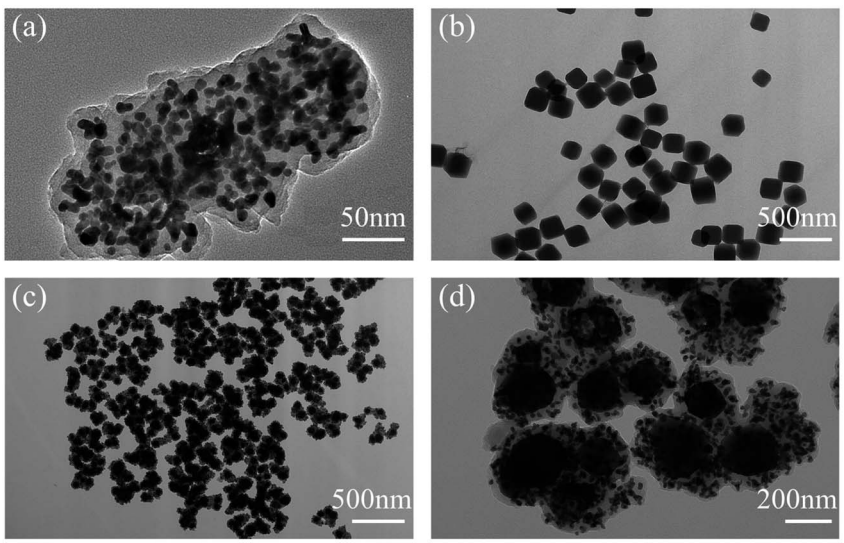

Fig. 3 TEM images of AuAg/PDA (a), ZIF-8 (b), and ZIF-8@AuAg/PDA (c and d).

$2\theta = 22°$, which is characteristic of the amorphous structure of SiO_2.[45] After the SiO_2 nanospheres have been coated with an AuAg/PDA shell layer, diffraction peaks appeared at 38.2°, 44.22°, 64.52°, and 77.54°, which can be classified as the (111), (200), (220), and (311) Au lattice planes (JCPDS card no. 04-0784). Due to the Au and Ag having a similar structure, they cannot be distinguished. Here, the diffraction peaks must originate from both Au and Ag, and thus the nanocrystals in the product are defined as AuAg bimetallic nanoparticles. Moreover, the SiO_2@AuAg/PDA, SiO_2@Au/PDA and SiO_2@Ag/PDA exhibit similar XRD patterns, which also agrees with the above analysis.

Thermogravimetric analysis (TGA) was further used to study the composition of the SiO_2@AuAg/PDA nanospheres (Fig. 4b). The weight losses of SiO_2, SiO_2/PDA, SiO_2@Au/PDA, SiO_2@Ag/PDA and SiO_2@AuAg/PDA are 3.03 wt%, 6.64 wt%, 8.95 wt%, 6.53 wt% and 9.33 wt%, respectively. PDA will decompose at high temperatures, so the weight loss of SiO_2/PDA is larger than that of SiO_2. On the other hand, the weight loss of SiO_2/PDA is small, indicating that the PDA shell is thin, which agrees with the above TEM analysis. The weight loss of SiO_2@AuAg/PDA is the largest, which may be related to the fact that AuAg bimetallic nanocrystals promote the polymerization of PDA.

Fig. 4c shows the FTIR patterns of SiO_2, SiO_2/PDA, SiO_2@Au/PDA, SiO_2@Ag/PDA, and SiO_2@AuAg/PDA. For SiO_2, a strong absorption peak at 1119 cm^{-1} appears, which can be assigned as the stretching vibration of Si–O–Si. For SiO_2@AuAg/PDA, the absorption peaks at 3440 cm^{-1}, 1623 cm^{-1} and 1403 cm^{-1} are attributed to the stretching vibrations of –OH/–NH_2, –O–H and –C–O in PDA. The Au and Ag do not show characteristic peaks in the FTIR; thus, SiO_2@Au/PDA, SiO_2@Ag/PDA, and SiO_2@AuAg/PDA have the same absorption spectra.

Fig. 4d shows the UV-vis absorption profiles of the different samples. As shown in the figure, the SiO_2 and SiO_2/PDA suspensions do not exhibit obvious characteristic peaks in the range of 250–1100 nm. In contrast, the characteristic peaks of SiO_2@Au/PDA and SiO_2@Ag/PDA are located at 650 nm and 450 nm, respectively, which indicates that the Au/PDA and Ag/PDA shell layers have been successfully immobilized on the SiO_2. In addition, SiO_2@AuAg/PDA has a full coverage of absorption peaks with higher absorbance than the other samples. The characteristic peak absorption is located at about 550 nm, indicating successful loading of AuAg bimetallic nanocrystals. Moreover, the absorption area is critically broadened to the near-infrared region, which demonstrates that the final product probably exhibits good photothermal behavior.

X-ray photoelectron spectroscopy (XPS) was used to analyze the surface chemical compositions and binding states of the SiO_2@AuAg/PDA nanospheres. As shown in Fig. 5a, C 1s (284.8 eV), O 1s (532.3 eV), and Si 2p (99.8 eV) peaks were clearly observed for SiO_2. The O 1s and Si 2p peaks were derived from SiO_2, while the C 1s was derived from the residue ethanol or

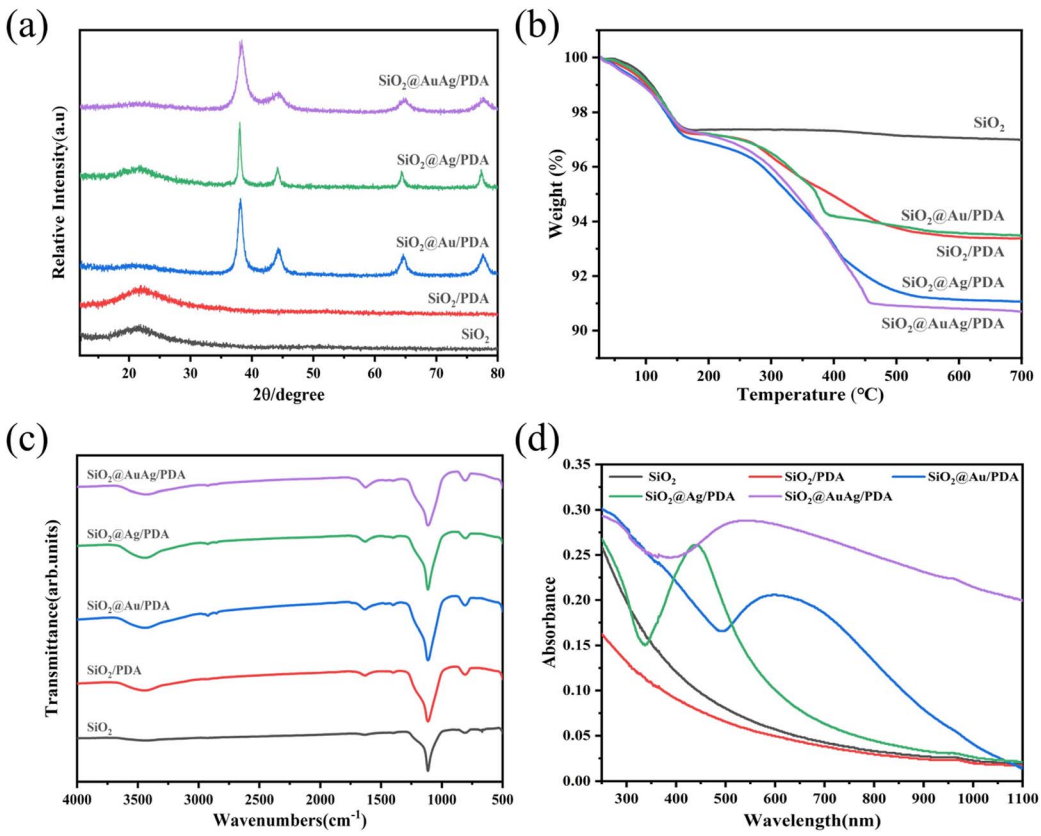

Fig. 4 (a) XRD diffraction patterns, (b) TG curves, (c) FTIR spectra and (d) UV-vis absorption spectra of SiO_2, SiO_2/PDA, SiO_2@Au/PDA, SiO_2@Ag/PDA and SiO_2@AuAg/PDA.

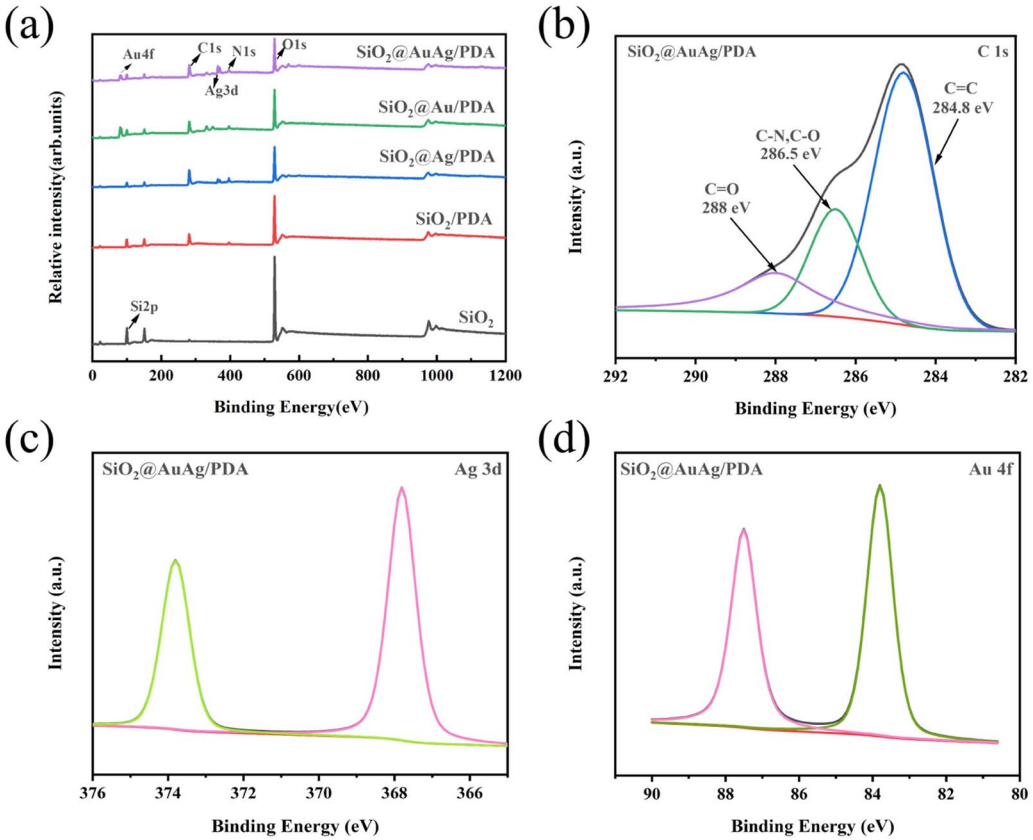

Fig. 5 (a) XPS of SiO_2, SiO_2/PDA, SiO_2@Ag/PDA, SiO_2@Au/PDA and SiO_2@AuAg/PDA; (b) C 1s, (c) Ag 3d and (d) Au 4f core-level spectra of SiO_2@AuAg/PDA.

organic groups of TEOS in the product. After coating with PDA, a clear N 1s peak (399.9 eV) appeared, indicating the presence of PDA. With the AuAg/PDA shell coated on the SiO_2, the Si 2p peak is significantly decreased because the detection depth of XPS is only 10 nm, which demonstrates that the SiO_2 was well-wrapped by the AuAg/PDA shell layer. In the C 1s spectrum, the characteristic C–N peak at 286.5 eV occupies a considerable proportion (Fig. 5b). In addition, Ag 3d (367.8 eV) and Au 4f (83.7 eV) peaks were detected, which further proves that the Au and Ag bimetallic nanocrystals were encapsulated within the PDA shell (Fig. 5c and d). Moreover, the XPS of the SiO_2@Au/PDA nanospheres and SiO_2@Ag/PDA nanospheres also indicated the successful immobilization of Au or Ag nanocrystals in the product, respectively.

In this work, the surface modification is important for the preparation of the core/shell nanostructure. Here, SiO_2@Au/PDA nanospheres synthesized with and without 3-aminopropyltriethoxysilane (APTES) modification were taken as an example. After the addition of dopamine hydrochloride buffer solution, under alkaline conditions, the $HAuCl_4$ reacted rapidly with DA and the solution showed a brick-red color, indicating the formation of Au nanocrystals. As shown in Fig. S2a and c,† Au/PDA nanoclusters attached to SiO_2 nanospheres were obtained, in which the Au nanocrystals formed clusters and were encapsulated within the PDA shell. The high magnification TEM image of an individual SiO_2@Au/PDA nanosphere is shown in Fig. S2e.† Clearly, cluster-like Au/PDA core/shell nanoparticles were randomly immobilized around the surface of SiO_2 and the average size of the cluster-like Au/PDA nanoparticles was 56–100 nm. In this case, APTES was used as a surface modifier for the SiO_2 nanospheres, and the amino group was grafted onto the surface of the nanospheres *via* chemical grafting to obtain SiO_2–NH_2. After the APTES modification, the Au/PDA shell layer could be effectively wrapped around the surface of SiO_2 to give the SiO_2@Au/PDA nanosphere. As shown in Fig. S2b and d,† the Au/PDA shell layer was uniformly coated on the SiO_2 and the shell thickness was about 20 nm. Fig. S2f† shows the high magnification TEM image of a SiO_2@Au/PDA nanosphere. Both the Au nanocrystals and SiO_2 nanosphere were well-encapsulated by the PDA, which indicated that the surface modification is important for the preparation.

3.2 Photothermal performance of the SiO_2@AuAg/PDA nanospheres

Fig. 6a shows the UV-vis-NIR absorption spectra of the SiO_2@AuAg/PDA nanospheres. With increasing concentration, the NIR absorption is relatively increased, which indicates the product possesses a potential photothermal behavior. Under NIR laser irradiation (808 nm, 2.5 W cm^{-2}), the temperature of the SiO_2@AuAg/PDA suspensions increased rapidly with increasing concentration and irradiation time. Fig. 6b shows the temperature changes of water,

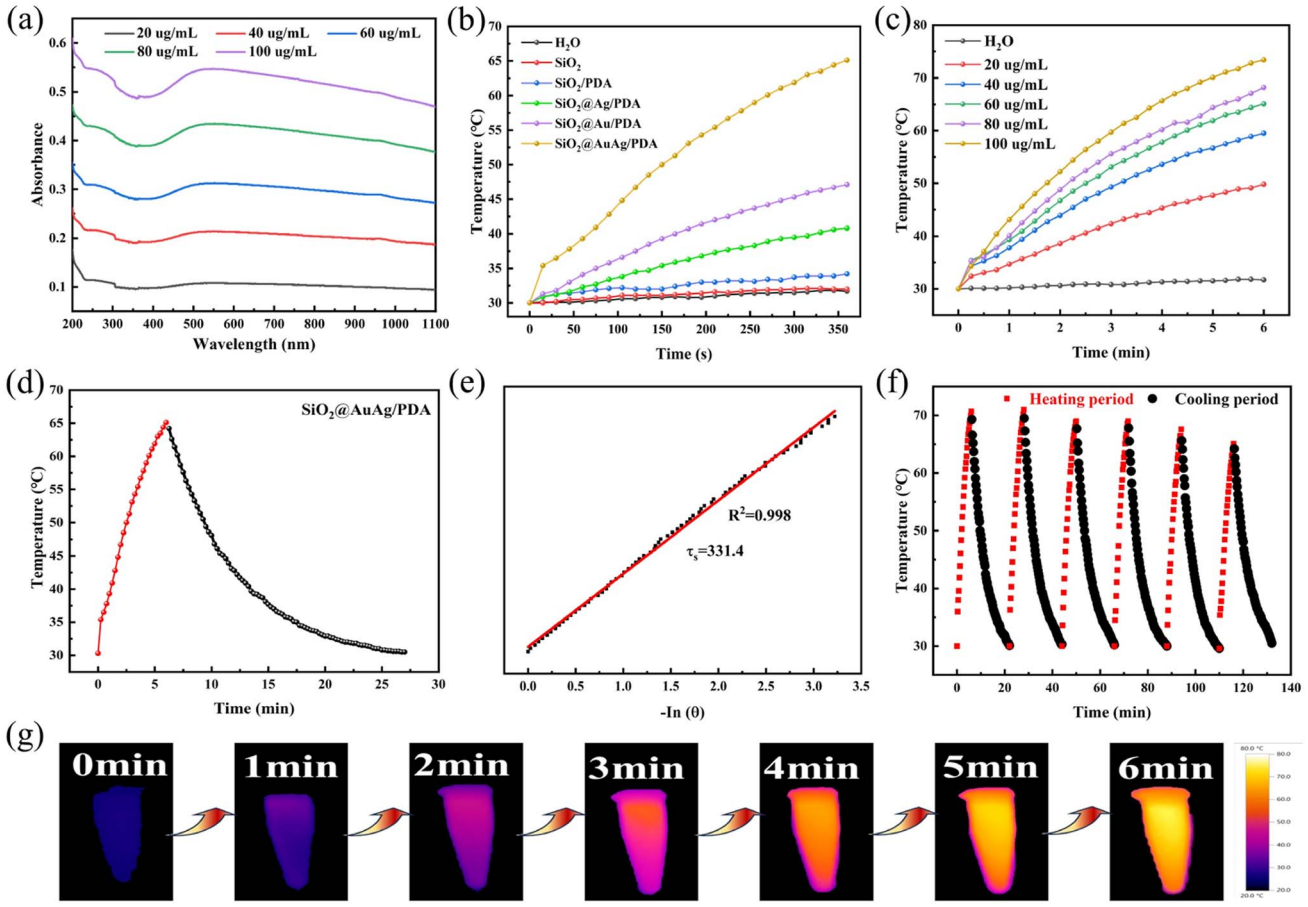

Fig. 6 (a) UV-Vis-NIR absorption spectra of SiO_2@AuAg/PDA nanospheres; (b) temperature elevation curves for DI water, SiO_2, SiO_2/PDA, SiO_2@Ag/PDA, SiO_2@Au/PDA and SiO_2@AuAg/PDA (average concentration 60 μg mL^{-1}), under NIR laser irradiation (808 nm, 2.5 W cm^{-2}); (c) temperature elevation curves for SiO_2@AuAg/PDA core–shell suspensions with various concentrations under NIR laser irradiation (808 nm, 2.5 W cm^{-2}); (d) heating and cooling profiles of SiO_2@AuAg/PDA nanosphere solution (60 μg mL^{-1}); (e) a plot fitting of cooling time *versus* $-\ln(\theta)$, where θ refers to a dimensionless driving force temperature; (f) temperature elevation curve of SiO_2@AuAg/PDA core/shell structure solution (60 μg mL^{-1}) with NIR laser on/off cycles; (g) infrared thermography of the SiO_2@AuAg/PDA suspension under NIR laser irradiation.

SiO_2, SiO_2/PDA, SiO_2@Ag/PDA, SiO_2@Au/PDA, and SiO_2@AuAg/PDA after irradiation with a NIR laser (808 nm, 2.5 W cm^{-2}) for 6 min to evaluate the photothermal conversion capability. The temperature changes of deionized water and the SiO_2 suspension were small and negligible, and SiO_2/PDA had a weak warming trend, which indicated that PDA had a low photothermal conversion effect. In contrast, the temperature changes of SiO_2@Ag/PDA, SiO_2@Au/PDA and SiO_2@AuAg/PDA after 6 min of 808 nm laser irradiation were very large, among which SiO_2@AuAg/PDA had the best photothermal effect of 65.1 °C. The photothermal effects of SiO_2@Au/PDA and SiO_2@Ag/PDA were almost the same and the temperatures were 47.1 °C and 40.8 °C, respectively. These results indicated that Au and Ag nanocrystals were the key factors for photothermal conversion. With increasing concentration, the temperature of SiO_2@AuAg/PDA increased and it could reach as high as 73.4°C. As shown in Fig. 6c, when the concentration of the SiO_2@AuAg/PDA nanosphere solution was increased from 20 μg mL^{-1} to 100 μg mL^{-1}, the temperature of the sample solution increased from 49.8 °C to 73.4 °C after irradiation with NIR light for 6 min. To further evaluate the photothermal conversion performance of the SiO_2@AuAg/PDA nanospheres, the test process profiles of heating and cooling were recorded (Fig. 6d). The photothermal conversion efficiency of SiO_2@AuAg/PDA was calculated to be 48.1% (Fig. 6e), indicating a strong photothermal conversion capability. Fig. 6f shows the photothermal stability of the sample solution, evaluated by controlling the NIR irradiation (808 nm, 2.5 W cm^{-2}) between on/off at room temperature. The temperature distributions of the sample solutions were similar over the 6 cycling cycles, and the results indicated that SiO_2@AuAg/PDA possessed good photothermal stability. In addition, the photothermal conversion performance of the SiO_2@AuAg/PDA nanospheres can be further directly visualized *via* IR thermography (Fig. 6g).

3.3 Photothermally enhanced catalytic activity of SiO_2@AuAg/PDA nanospheres for reducing 4-nitrophenol

Due to the presence of AuAg bimetallic nanocrystals, the SiO_2@AuAg/PDA nanospheres have good catalytic properties. 4-Nitrophenol is characterized by difficult degradation and high

stability, and it is an important pollutant in industrial wastewater. Therefore, the catalytic activity of SiO_2@AuAg/PDA was evaluated by using 4-nitrophenol as a model.

As shown in Fig. 7a, 4-nitrophenol has a characteristic absorption peak at 317 nm, and the solution was light yellow in color. After the addition of $NaBH_4$, 4-nitrophenol generates 4-

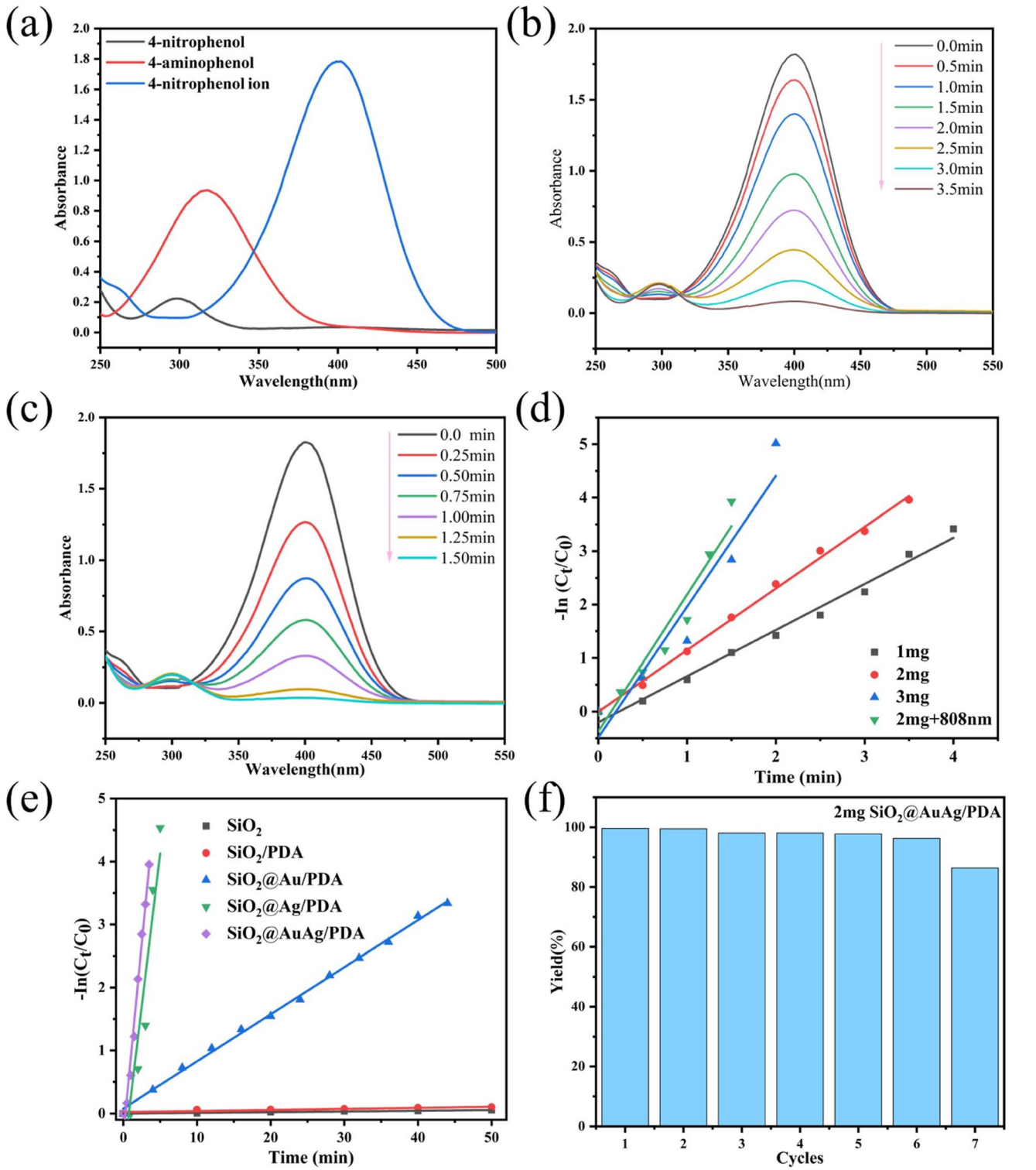

Fig. 7 UV-Vis absorption spectra of 4-nitrophenol, 4-aminophenol and 4-nitrophenol ions (a); UV-Vis spectra of the reaction of 4-nitrophenol catalyzed by 2 mg SiO_2@AuAg/PDA nanospheres (b) and UV-Vis spectra of the reaction of 4-nitrophenol catalyzed under NIR laser (808 nm, 2.5 W cm^{-2}) irradiation (c). Linear relationships between $\ln(C_t/C_0)$ and reaction time for the SiO_2@AuAg/PDA nano-catalyst at different weights (d). Linear relationship between $\ln(C_t/C_0)$ and time for SiO_2, SiO_2/PDA, SiO_2@Au/PDA, SiO_2@Ag/PDA and SiO_2 @AuAg/PDA (average weight 2 mg) nanocatalysts (e). Catalyst recovery study (f).

Table 1 SiO_2@AuAg/PDA-catalyzed reduction of pollutants compared to reported catalysts

Substrate	Catalyst	Time (min)	Ref.
4-NP	Ag/MgO	6.7	50
	KCC-1/Au	12	51
	Au-GO	30	52
	Ag/TiO_2–Cu	25	53
	Au/graphene hydrogel	12	54
	SiO_2@AuAg/PDA + NIR	1.75	This work

nitrophenol ion and the absorption peak was shifted right to 400 nm. When the catalyst was further added, 4-aminophenol was obtained and the solution showed a transparent color with an increased absorption peak at 300 nm. The formation of the target product could be further confirmed by the infrared spectroscopic data from Kate *et al.*[46] In our experiment, 2 mg SiO_2@AuAg/PDA nanospheres were added in the reaction and the absorption peak at 400 nm gradually diminished, while at the same time the new absorption peak at 300 nm appeared, which corresponded to the conversion of 4-nitrophenol ions to 4-aminophenol. Eventually, the characteristic peak at 400 nm disappeared completely, while the absorption peak at 300 nm no longer increased, indicating the end of the reaction. The time required for the whole reaction process was 3.5 min, indicating quick reaction kinetics (Fig. 7b).

Interestingly, the catalytic reaction can be made faster by applying NIR (808 nm) irradiation. As shown in Fig. 7c, the reaction time was drastically shortened (57%), which indicates that the NIR treatment significantly improves the catalytic kinetics. Fig. 7d shows the linear relationship between $\ln(C_t/C_0)$ and reaction time t for different catalyst qualities under different reaction conditions, where C_t represents the concentration of 4-nitrophenol at moment t and C_0 represents the initial concentration of 4-nitrophenol. The reaction rate constants for the reduction of 4-nitrophenol to 4-aminophenol with different masses (1 mg, 2 mg and 3 mg) of SiO_2@AuAg/PDA nanocatalyst as well as for the NIR (808 nm, 2.5 W cm^{-2}) treatment group (with 2 mg catalyst) were 0.862 min^{-1}, 1.152 min^{-1}, 2.448 min^{-1} and 2.559 min^{-1}, respectively. In addition, the reaction rate constants with the weight ratios of the nanosphere catalyst were calculated to be 0.862 min^{-1} mg^{-1}, 0.576 min^{-1} mg^{-1} and 0.816 min^{-1} mg^{-1}. After NIR (2 mg + 808 nm) treatment, the value of the reaction rate constant k reaches 1.279 min^{-1} mg^{-1}, which indicates that the photothermal effect greatly enhances the catalytic process.

Similarly, as shown in Fig. 7e, the reaction rate constants for different samples (SiO_2, SiO_2/PDA, SiO_2@Au/PDA, SiO_2@Ag/PDA and SiO_2@AuAg/PDA) at the same weight (2 mg) were also tested and the values were 1.15×10^{-3} min^{-1}, 1.71×10^{-3} min^{-1}, 0.074 min^{-1}, 0.972 min^{-1} and 1.217 min^{-1}, respectively. The ratios of reaction rate constant to weight are 0.475×10^{-3} min^{-1} mg^{-1}, 0.575×10^{-3} min^{-1} mg^{-1}, 3.7×10^{-2} min^{-1} mg^{-1}, 0.486 min^{-1} mg^{-1} and 0.608 min^{-1} mg^{-1}. It can be found that the presence of SiO_2@AuAg/PDA nanospheres in the catalytic reaction is the key factor and the AuAg bimetallic nanocrystals show the best synergistic effect. Fig. 7f shows the cyclic catalytic activity of the SiO_2@AuAg/PDA nanospheres. After 7 cycles of catalytic reaction, the catalyst still maintains a high catalytic activity (more than 86%). This is similar to previously reported results.[47] The PDA shell layer attached to the

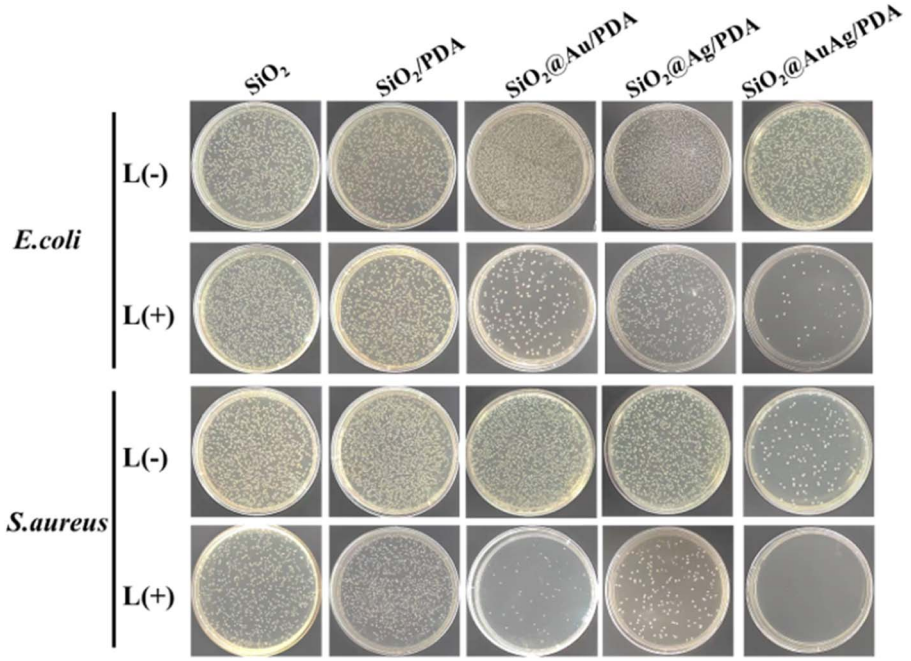

Fig. 8 Images of bacteria colonies formed by *E. coli* and *S. aureus* treated with SiO_2, SiO_2/PDA, SiO_2@Au/PDA, SiO_2@Ag/PDA and SiO_2@AuAg/PDA (60 μg mL^{-1}) with or without NIR irradiation for 6 min (808 nm, 2.5 W cm^{-2}).

surface of the AuAg nanoparticles slows down the oxidation process and improves the stability of the metal nanoparticles, which is conducive to the separation and possible recycling of catalysts. The small reduction at the 7th cycle must result from leakage of the AuAg nanoparticles during separation.[48] The results show that the catalyst surface remains active during successive cycles.[49] A comparison of this catalyst with other reported catalysts is provided in Table 1.

To further detect the catalytic performance, the infrared profiles of 4-nitrophenol and its reduction product 4-aminophenol were characterized (Fig. S3†). For 4-nitrophenol, two absorption peaks appear at 1342 cm^{-1} and 1498 cm^{-1}, corresponding to N=O and N–O stretching vibrations, respectively. For 4-aminophenol, two absorption peaks appeared at 864 cm^{-1} and 1636 cm^{-1}, attributed to N–H stretching vibrations.

3.4 "Photothermal–Ag^+" coupled antimicrobial properties of SiO_2@AuAg/PDA nanospheres

The antimicrobial properties of different samples (SiO_2, SiO_2/PDA, SiO_2@Au/PDA, SiO_2@Ag/PDA and SiO_2@AuAg/PDA) were further measured. Fig. 8 shows the optical images of each group of samples incubated with *E. coli* and *S. aureus*. The results show that the SiO_2@AuAg/PDA group (60 μg mL^{-1}) displayed a clear inactivation of *S. aureus* without NIR light treatment, which may be related to the release of Ag^+ under high-concentration conditions. After treatment with near-infrared light (808 nm, 2.5 W cm^{-2}), the antimicrobial effect of the SiO_2/PDA group was weaker, which must be due to the low photothermal effect induced by PDA. In addition, both the SiO_2@Au/PDA and SiO_2@Ag/PDA groups showed unique antibacterial effects; the former originates from the good photothermal effect of the metal ions, and the latter might be due to the promotion of Ag^+ release by NIR treatment.

Most importantly, the antibacterial effect of the SiO_2@AuAg/PDA group was the best, and an ultra-low dose of Ag^+ ions could effectively disrupt the bacterial membranes, which led to an increase in the permeability and a decrease in the heat-resistance of the cell membrane. On the other hand, thermotherapy can trigger the release of more Ag^+, which further improves the bactericidal efficiency of chemothermal therapy.[55–57] As the concentration of SiO_2@AuAg/PDA nanospheres increased, the antibacterial effect became more and more significant. As shown in Fig. 9, when the concentration was 60 μg mL^{-1}, almost all of the *S. aureus* was inactivated, while when the concentration was 90 μg mL^{-1}, all of the bacteria were inactivated. The different degrees of bactericidal effect on the two kinds of bacteria might be related to the difference in the structure of the bacterial cell wall.

Fig. 10 shows a schematic illustration of the photothermal antimicrobial process of the SiO_2@AuAg/PDA nanospheres. Under weak alkaline conditions, the dopamine molecules undergo self-polymerization, which leads to the easy deposition of polydopamine (PDA) on the surface of the template SiO_2, improving the stability and biocompatibility of the composite without any significant effect on bacteria. Under NIR treatment, the SiO_2@Au/PDA nanospheres convert the light energy into heat energy due to their good photothermal properties, thereby destroying the protein structure of the bacteria and ultimately killing them (Fig. 10a). However, to better kill bacteria *via* photothermal therapy, a higher temperature is usually required, thus limiting its practical application. Ag^+ is known to have broad-spectrum antibacterial activity, but this is weak in the absence of NIR treatment. Once NIR irradiation is introduced,

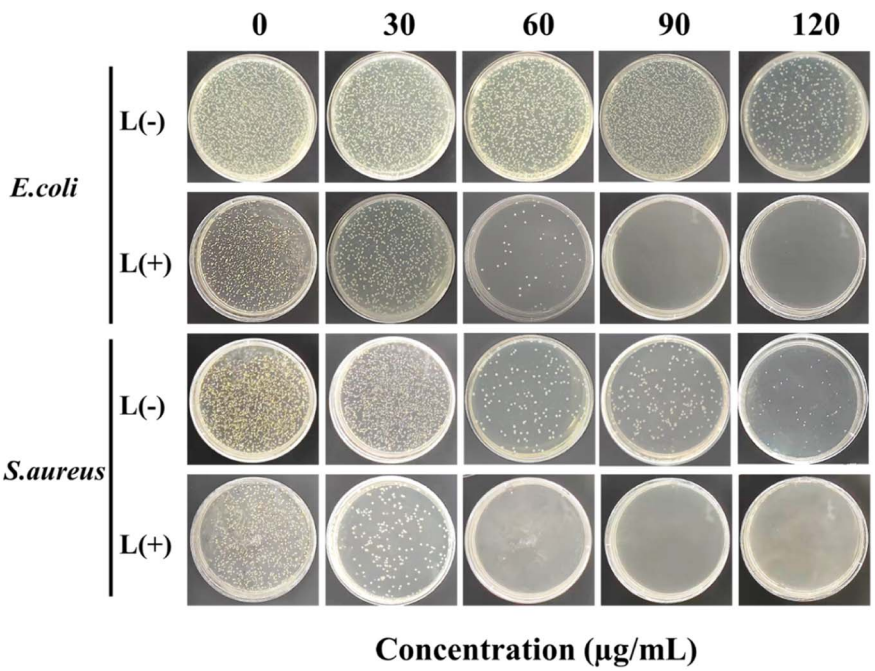

Fig. 9 Images of bacteria colonies formed by *E. coli* and *S. aureus* treated with SiO_2@AuAg/PDA (0, 30, 60, 90 and 120 μg mL^{-1}) with or without NIR irradiation for 6 min (808 nm, 2.5 W cm^{-2}).

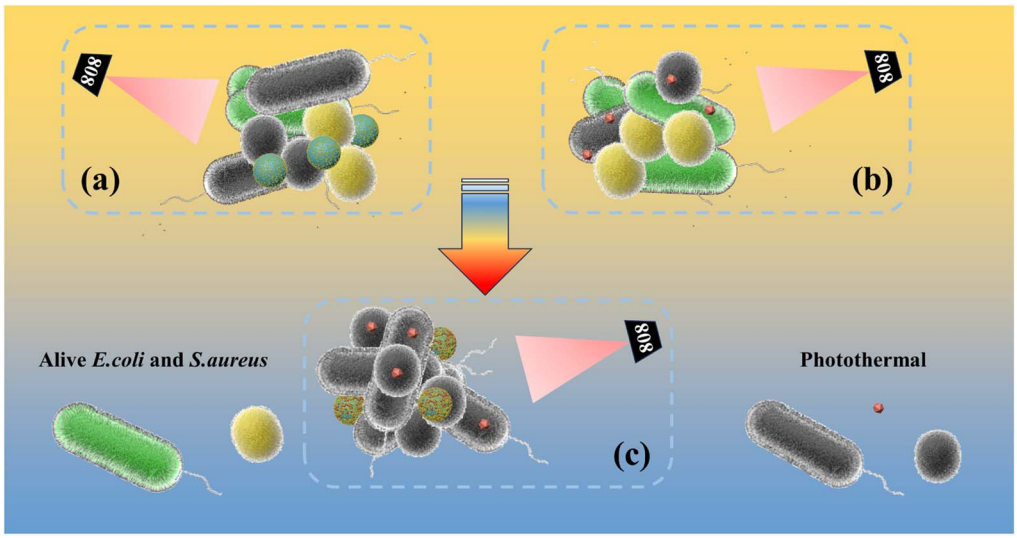

Fig. 10 Illustration of the interaction between particles and bacteria in the antibacterial process. Schematic diagram of antimicrobial activity under (a) Au nanocrystal photothermal, (b) Ag^+-release–photothermal, and (c) bimetallic Ag^+-release–photothermal coupled conditions.

Ag^+ release is also promoted during the photothermal process, making it more helpful to kill bacteria (Fig. 10b). As a result, an "Ag^+ release–photothermal" synergistic antibacterial effect was carried out and the coupled behavior showed exciting bactericidal effects. Finally, the SiO_2@AuAg/PDA nanospheres have good photothermal properties and they are more destructive to bacteria. According to the related literature,[58] the synergistic effect of two elements, bimetallic gold and silver, outperforms monometallic nanoclusters. Moreover, the AuAg bimetallic nanoclusters possess higher antibacterial efficiency compared to the monometallic nanoclusters. In conclusion, the "Ag^+-release–photothermal" coupled sterilization method has great potential in nanomedicine.

4. Conclusion

In this work, we report a simple method for the preparation of SiO_2@AuAg/PDA core/shell hybrid nanospheres *via in situ* redox polymerization. The AuAg bimetallic nanoparticles were well-encapsulated by the PDA layer, which could effectively prevent their leaching during the catalytic reaction. Due to the synergistic effect of the AuAg bimetallic nanoparticles, the SiO_2@AuAg/PDA nanospheres exhibited good catalytic activity, with the catalytic kinetics being improved by 2.2 times under near-infrared irradiation. In addition to the inherent bactericidal effect of released Ag^+, the SiO_2@AuAg/PDA nanospheres showed good photothermal antimicrobial activity against Gram-negative bacteria (*E. coli*) and Gram-positive bacteria (*S. aureus*). Importantly, all the bacteria could be inactivated at a concentration of 90 μg mL^{-1}. As a result, due to the non-traditional "Ag^+-release–photothermal" synergistic antibacterial function and NIR-improved catalytic activity, this material is expected to be widely used in industrial, agricultural, environmental and medical applications.

Author contributions

Dazheng Ci: conceptualization, investigation, methodology, visualization, writing – original draft. Ning Wang: investigation, methodology, supervision, funding acquisition. Yunqi Xu: visualization, supervision. Shanshan Wu: formula derivation. Jing Wang: visualization. Haoran Li: visualization. Shouhu Xuan: supervision, visualization. Qunling Fang: resources, supervision, project administration, funding acquisition.

Conflicts of interest

The authors declare no conflict of interest.

Acknowledgements

National Natural Science Foundation of China (Grant number 81703449) and the Fundamental Research Funds for the Central Universities (PA2020GDKC0005).

References

1 H. Lv, M. Lin, C. Yu, H. Wang, M. Li, L. Zhang, Z. Liu and Z. Chen, Pd decorated MoS_2 nanoflowers as photothermal catalyst for enhanced NIR-induced 4-nitrophenol reduction, *J. Environ. Chem. Eng.*, 2023, **11**(5), 110375.
2 M. Mamera, J. Van and M. Aghoghovwia, Treatment of faecal sludge and sewage effluent by pinewood biochar to reduce wastewater bacteria and inorganic contaminants leaching, *Water Res.*, 2022, **221**, 118775.
3 N. Yılmaz, T. Baran and M. Çalışkan, Production of Pd nanoparticles embedded on micro-sized chitosan/graphitic carbon nitride hybrid spheres for treatment of environmental pollutants in aqueous medium, *Ceram. Int.*, 2021, **47**(19), 27736–27747.

4 S. Zhang, J. Wang, Y. Zhang, J. Ma, L. Huang, S. Yu, L. Chen, G. Song, M. Qiu and X. Wang, Applications of water-stable metal-organic frameworks in the removal of water pollutants: a review, *Environ. Pollut.*, 2021, **291**, 118076.
5 M. Frieri, K. Kumar and A. Boutin, Antibiotic resistance, *J. Infect. Public Health*, 2017, **10**(4), 369–378.
6 S. Li, B. Ondon, S. Ho, J. Jiang and F. Li, Antibiotic resistant bacteria and genes in wastewater treatment plants: from occurrence to treatment strategies, *Sci. Total Environ.*, 2022, **838**(4), 156544.
7 S. Shao, Y. Hu, J. Cheng and Y. Chen, Research progress on distribution, migration, transformation of antibiotics and antibiotic resistance genes (ARGs) in aquatic environment, *Crit. Rev. Biotechnol.*, 2018, **38**(8), 1195–1208.
8 M. Chang, Z. Hou, M. Wang, C. Yang, R. Wang, F. Li, D. Liu, T. Peng, C. Li and J. Lin, Single-atom Pd nanozyme for ferroptosis-boosted mild-temperature photothermal therapy, *Angew. Chem., Int. Ed.*, 2021, **60**(23), 12971–12979.
9 J. Pickering, V. Bhethanabotla and J. Kuhn, Plasmonic photocatalytic reactor design: use of multilayered films for improved organic degradation rates in a recirculating flow reactor, *Chem. Eng. J.*, 2017, **314**, 11–18.
10 J. Qiu, T. Yang, Y. Li, W. Qian and X. Liu, Au@Ag@Pt core–shell nanorods regulating Ag release behavior endow titanium antibacterial activity and biocompatibility, *Rare Met.*, 2022, **41**(2), 630–638.
11 J. Yan, H. Sun, J. Li, W. Qi and H. Wang, A theranostic plaster combining photothermal therapy and photodynamic therapy based on chlorin e6/gold nanorods (Ce6/Au nrs) composite, *Colloids Surf., A*, 2018, **537**, 460–466.
12 L. He, L. Lv, S. Pillai, H. Wang, J. Xue, Y. Ma, Y. Liu, Y. Chen, L. Wu, Z. Zhang and L. Yang, Efficient degradation of diclofenac sodium by periodate activation using Fe/Cu bimetallic modified sewage sludge biochar/UV system, *Sci. Total Environ.*, 2021, **783**, 146974.
13 R. Liu, J. Guo, G. Ma, P. Jiang, D. Zhang, D. Li, L. Chen, Y. Guo and G. Ge, Alloyed crystalline Au-Ag hollow nanostructures with high chemical stability and catalytic performance, *ACS Appl. Mater. Interfaces*, 2016, **8**(26), 16833–16844.
14 M. Marimuthu, H. Li and Q. Chen, Facile ultrasonic synthesis of silver-based bimetal nanoparticles for efficient catalytic reduction of 4-nitrophenol, *J. Mol. Liq.*, 2021, **333**, 115963.
15 Y. Sun, Z. Yang, P. Tian, Y. Sheng, J. Xu and Y. Han, Oxidative degradation of nitrobenzene by a fenton-like reaction with Fe-Cu bimetallic catalysts, *Appl. Catal., B*, 2019, **244**, 1–10.
16 G. Liao, Y. Gong, L. Zhong, J. Fang, L. Zhang, Z. Xu, H. Gao and B. Fang, Unlocking the door to highly efficient Ag-based nanoparticles catalysts for $NaBH_4$-assisted nitrophenol reduction, *Nano Res.*, 2019, **12**(10), 2407–2436.
17 A. Deshmukh and B. Kim, Flower-like biogenic gold nanostructures for improved catalytic reduction of 4-nitrophenol, *J. Environ. Chem. Eng.*, 2021, **9**(6), 106707.
18 S. Fu, C. Zhu, J. Song, M. Engelhard, X. Li, D. Du and Y. Lin, Highly ordered mesoporous bimetallic phosphides as efficient oxygen evolution electrocatalysts, *ACS Energy Lett.*, 2016, **1**(4), 792–796.
19 X. Zhang, R. Shen, X. Guo, X. Yan, Y. Chen, J. Hu and W. Lang, Bimetallic Ag-Cu nanoparticles anchored on polypropylene (PP) nonwoven fabrics: superb catalytic efficiency and stability in 4-nitrophenol reduction, *Chem. Eng. J.*, 2021, **408**, 128018.
20 H. Yu, W. Tang, K. Li, S. Zhao, H. Yin and S. Zhou, Enhanced catalytic performance for hydrogenation of substituted nitroaromatics over Ir-based bimetallic nanocatalysts, *ACS Appl. Mater. Interfaces*, 2019, **11**(7), 6958–6969.
21 X. Liao, F. Yang, R. Wang, X. He, H. Li, R. Kao, W. Xia and H. Sun, Identification of catabolite control protein A from staphylococcus aureus as a target of silver ions, *Chem. Sci.*, 2017, **8**(12), 8061–8066.
22 X. Bai, Y. Yang, W. Zheng, Y. Huang, F. Xu and Z. Bao, Synergistic photothermal antibacterial therapy enabled by multifunctional nanomaterials: progress and perspectives, *Mater. Chem. Front.*, 2023, **7**(3), 355–380.
23 S. Sasidharan, R. Poojari, D. Bahadur and R. Srivastava, Embelin-mediated green synthesis of quasi-spherical and star-shaped plasmonic nanostructures for antibacterial activity, photothermal therapy, and computed tomographic imaging, *ACS Sustain. Chem. Eng.*, 2018, **6**(8), 10562–10577.
24 Y. Shi, J. Yin, Q. Peng, X. Lv, Q. Li, D. Yang, X. Song, W. Wang and X. Dong, An acidity-responsive polyoxometalate with inflammatory retention for NIR-II photothermal-enhanced chemodynamic antibacterial therapy, *Biomater. Sci.*, 2020, **8**(21), 6093–6099.
25 Y. Xu, K. Wang, S. Zhao, Q. Xiong, G. Liu, Y. Li, Q. Fang, X. Gong and S. Xuan, Rough surface $NiFe_2O_4$@Au/Polydopamine with a magnetic field enhanced photothermal antibacterial effect, *Chem. Eng. J.*, 2022, **437**, 135282.
26 J. Jia, G. Liu, W. Xu, X. Tian, S. Li, F. Han, Y. Feng, X. Dong and H. Chen, Fine-tuning the homometallic interface of Au-on-Au nanorods and their photothermal therapy in the NIR-II window, *Angew. Chem., Int. Ed.*, 2020, **59**(34), 14443–14448.
27 E. Park, R. Selvaraj and Y. Kim, High-efficiency photothermal sterilization on PDMS film with Au@CuS yolk-shell nanoparticles, *J. Ind. Eng. Chem.*, 2022, **113**, 522–529.
28 G. Liu, Q. Xiong, Y. Xu, Q. Fang, K. Leung, M. Sang, S. Xuan and L. Hao, Sandwich-structured MXene@Au/polydopamine nanosheets with excellent photothermal-enhancing catalytic activity, *Colloids Surf., A*, 2022, **633**, 127860.
29 Z. Lv, S. He, Y. Wang and X. Zhu, Noble metal nanomaterials for NIR-triggered photothermal therapy in cancer, *Adv. Healthcare Mater.*, 2021, **10**(6), e2001806.
30 X. Chen, S. Ku, J. Weibel, E. Ximenes, X. Liu, M. Ladisch and S. Garimella, Enhanced antimicrobial efficacy of bimetallic porous CuO microspheres decorated with Ag nanoparticles, *ACS Appl. Mater. Interfaces*, 2017, **9**(45), 39165–39173.
31 D. Kim, K. Park, J. Park and I. Choi, Photoactive MOF-derived bimetallic silver and cobalt nanocomposite with

enhanced antibacterial activity, *ACS Appl. Mater. Interfaces*, 2023, **15**(19), 22903–22914.

32 A. Jin, Y. Wang, K. Lin and L. Jiang, Nanoparticles modified by polydopamine: working as drug carriers, *Bioact. Mater.*, 2020, **5**(3), 522–541.

33 L. Liang, T. Hou, Q. Ouyang, L. Xie, S. Zhong, P. Li, S. Li and C. Li, Antimicrobial sodium alginate dressing immobilized with polydopamine-silver composite nanospheres, *Composites, Part B*, 2020, **188**, 107877.

34 I. I. Niyonshuti, V. Krishnamurthi, D. Okyere, L. Song, M. Benamara, X. Tong, Y. Wang and J. Chen, Polydopamine surface coating synergizes the antimicrobial activity of silver nanoparticles, *ACS Appl. Mater. Interfaces*, 2020, **12**(36), 40067–40077.

35 Y. Zhu, Y. Sun, J. Wang and B. Yu, Antimicrobial and antifouling surfaces through polydopamine bio-inspired coating, *Rare Met.*, 2022, **41**(2), 499–518.

36 N. Olteanu, C. Lazăr, A. Petcu, A. Meghea, E. Rogozea and M. Mihaly, One-pot synthesis of fluorescent Au@SiO_2 and SiO_2@Au nanoparticles, *Arabian J. Chem.*, 2016, **9**(6), 854–864.

37 J. Zhang, G. Lu and C. Cai, Regio- and stereoselective hydrosilylation of alkynes catalyzed by SiO_2 supported Pd–Cu bimetallic nanoparticles, *Green Chem.*, 2017, **19**(11), 2535–2540.

38 S. Mallakpour, E. Nikkhoo and C. Hussain, Application of MOF materials as drug delivery systems for cancer therapy and dermal treatment, *Coord. Chem. Rev.*, 2022, **451**, 214262.

39 C. Vaitsis, G. Sourkouni and C. Argirusis, Metal organic frameworks (MOFs) and ultrasound: a review, *Ultrason. Sonochem.*, 2019, **52**, 106–119.

40 P. Bazuła, P. Arnal, C. Galeano, B. Zibrowius, W. Schmidt and F. Schüth, Highly microporous monodisperse silica spheres synthesized by the Stöber process, *Microporous Mesoporous Mater.*, 2014, **200**, 317–325.

41 H. Lin, S. Gao, C. Dai, Y. Chen and J. Shi, A two-dimensional biodegradable niobium carbide (MXene) for photothermal tumor eradication in NIR-I and NIR-II biowindows, *J. Am. Chem. Soc.*, 2017, **139**(45), 16235–16247.

42 V. Jawale, G. Gugale, M. Chaskar, S. Pandit, R. Pawar, S. Suryawanshi, V. Pandit, G. Umarji and S. Arbuj, Two- and three-dimensional zinc oxide nanostructures and its photocatalytic dye degradation performance study, *J. Mater. Res.*, 2021, **36**(7), 1573–1583.

43 V. Jawale, A. Al-fahdawi, S. Salve, S. Pandit, G. Dawange, G. Gugale, M. Chaskar, D. Hammiche, S. Arbuj and V. Pandit, 6, 13-pentacenequinone/zinc oxide nanocomposites for organic dye degradation, *Mater. Today: Proc.*, 2022, **52**, 17–20.

44 Q. Fang, J. Zhang, L. Bai, J. Duan, H. Xu, K. Cham and S. Xuan, *In situ* redox-oxidation polymerization for magnetic core-shell nanostructure with polydopamine-encapsulated-Au hybrid shell, *J. Hazard. Mater.*, 2019, **367**, 15–25.

45 H. Zhang, D. Ke, L. Cheng, X. Feng, X. Hou, J. Wang, Y. Li and S. Han, CoPt-Co hybrid supported on amino modified SiO_2 nanospheres as a high performance catalyst for hydrogen generation from ammonia borane, *Prog. Nat. Sci.: Mater. Int.*, 2019, **29**(1), 1–9.

46 P. Kate, V. Pandit, V. Jawale and M. Bachute, L-Proline catalyzed one-pot three-component synthesis and evaluation for biological activities of tetrahydrobenzo[b]pyran: evaluation by green chemistry metrics, *J. Chem. Sci.*, 2022, **134**, 4.

47 Z. Moradi and A. Ghorbani, Fe_3O_4@SiO_2@KIT-6@2-ATP@CuI as a catalyst for hydration of benzonitriles and reduction of nitroarenes, *Sci. Rep.*, 2023, **13**(1), 7645.

48 B. Zhao, Z. Dong, Q. Wang, Y. Xu, N. Zhang, W. Liu, F. Lou and Y. Wang, Highly efficient mesoporous core-shell structured Ag@SiO_2 nanosphere as an environmentally friendly catalyst for hydrogenation of nitrobenzene, *Nanomaterials*, 2020, **10**(5), 883.

49 P. Chhattise, S. Saleh, V. Pandit, S. Arbuj and V. Chabukswar, ZnO nanostructures: a heterogeneous catalyst for the synthesis of benzoxanthene and pyranopyrazole scaffolds *via* a multi-component reaction strategy, *Mater. Adv.*, 2020, **1**(7), 2339–2345.

50 M. Nasrollahzadeh, R. Akbari, Z. Issaabadi and S. Sajadi, Biosynthesis and characterization of Ag/MgO nanocomposite and its catalytic performance in the rapid treatment of environmental contaminants, *Ceram. Int.*, 2020, **46**(2), 2093–2101.

51 H. Yang, S. Li, X. Zhang, X. Wang and J. Ma, Imidazolium ionic liquid-modified fibrous silica microspheres loaded with gold nanoparticles and their enhanced catalytic activity and reusability for the reduction of 4-nitrophenol, *J. Mater. Chem. A*, 2014, **2**(30), 12060.

52 Y. Choi, H. Bae, E. Seo, S. Jang, K. Park and B. Kim, Hybrid gold nanoparticle-reduced graphene oxide nanosheets as active catalysts for highly efficient reduction of nitroarenes, *J. Mater. Chem.*, 2011, **21**(39), 15431.

53 A. Hernández and V. González, Silver nanoparticles loaded on Cu-doped TiO_2 for the effective reduction of nitro-aromatic contaminants, *Chem. Eng. J.*, 2015, **261**, 53–59.

54 J. Li, C. Liu and Y. Liu, Au/graphene hydrogel: synthesis, characterization and its use for catalytic reduction of 4-nitrophenol, *J. Mater. Chem.*, 2012, **22**(17), 8426.

55 M. Liu, D. He, T. Yang, W. Liu, L. Mao, Y. Zhu, J. Wu, G. Luo and J. Deng, An efficient antimicrobial depot for infectious site-targeted chemo-photothermal therapy, *J. Nanobiotechnol.*, 2018, **16**(1), 23.

56 H. Wang, D. Wang, H. Huangfu, S. Chen, Q. Qin, S. Ren, Y. Zhang, L. Fu and Y. Zhou, Highly efficient photothermal branched Au-Ag nanoparticles containing procyanidins for synergistic antibacterial and anti-inflammatory immunotherapy, *Biomater. Sci.*, 2023, **11**(4), 1335–1349.

57 K. Zhou, Z. Zhang, J. Xue, J. Shang, D. Ding, W. Zhang, Z. Liu, F. Yan and N. Cheng, Hybrid Ag nanoparticles/polyoxometalate-polydopamine nano-flowers loaded chitosan/gelatin hydrogel scaffolds with synergistic photothermal/chemodynamic/Ag(+) anti-bacterial action for accelerated wound healing, *Int. J. Biol. Macromol.*, 2022, **221**, 135–148.

58 Q. Zhai, H. Xing, X. Zhang, J. Li and E. Wang, Enhanced electrochemiluminescence behavior of gold-silver bimetallic nanoclusters and its sensing application for mercury(II), *Anal. Chem.*, 2017, **89**(14), 7788–7794.